U N I V E R S I T À   D E G L I   S T U D I   D I   B E R G A M O

Dipartimento di Ingegneria - Technical Report n. 06/2002

ON THE KINEMATICS OF PORTEVIN-LE CHATELIER DEFORMATION BANDS: THEORETICAL MODELING AND NUMERICAL RESULTS

Peter HÄHNER and Egidio RIZZI

Subject Area: Mechanics

Dipartimento di Ingegneria

Redazione:

Dipartimento di Ingegneria
Università degli Studi di Bergamo
Viale Marconi 5
24044 Dalmine (BG)
tel.: +39 035 205 2300
fax: +39 035 562 779
http://dipinge.unibg.it

Responsabile:

Egidio Rizzi
e-mail: erizzi@unibg.it
tel.: +39 035 205 2325

Segreteria del Dipartimento:

Grazia Nava
e-mail: graziana@unibg.it
tel.: +39 035 205 2307

La Redazione ottempera agli obblighi previsti dall'Art. 1 del D.L.L. 31.08.1945, n. 660 e successive modifiche.

Le richieste di copie della presente pubblicazione vanno indirizzate ai relativi Autori o alla Redazione.

Le pubblicazioni del Dipartimento di Ingegneria dell'Università degli Studi di Bergamo mirano a fornire la tempestiva divulgazione degli esiti di ricerche scientifiche originali già concluse o ancora in corso.

On the kinematics of Portevin–Le Chatelier deformation bands: theoretical modeling and numerical results*

Peter HÄHNER[1], Egidio RIZZI[2]

Abstract

A model is presented for the description of the Portevin–Le Chatelier (PLC) effect, namely the oscillatory plastic yielding that may be observed in metal alloy specimens for certain ranges of the applied stress/strain rates and testing temperatures. The phenomenological model is based on the underlying microstructural Dynamic Strain Ageing (DSA), i.e. the dynamic interaction between mobile dislocations and diffusing solute atoms. Both time and space couplings are taken into account. Focus is made on Type A PLC instabilities, that is single PLC bands that nucleate and propagate smoothly throughout the tensile specimen as solitary plastic waves. The kinematics of these PLC bands is first studied analytically, based on some simplifying assumptions, and then validated numerically by a Finite Differences integration of the model equations. The characteristics of the PLC bands, that is band speed, band width and band plastic strain are filtered out automatically from the space–time fields of plastic activity. The band parameters exhibit very good matching with the theoretical results and order-of-magnitude agreement with the experimental observation of the PLC effect.

Key words: material instabilities, strain localization, Portevin–Le Chatelier effect (PLC), Dynamic Strain Ageing (DSA), strain-rate softening, PLC bands, solitary plastic waves.

Work performed jointly by the authors at the Technische Universität Braunschweig, Institut für Metallphysik und Nukleare Festkörperphysik, Germany.

[1]European Commission, DG-Joint Research Centre, Mechanical Performance Characterization, Institute for Energy, PO Box 2, NL-1755 ZG Petten, The Netherlands.

[2]Università degli Studi di Bergamo, Facoltà di Ingegneria di Dalmine, Dipartimento di Ingegneria, viale G. Marconi 5, I-24044 Dalmine (BG), Italy.

1 Introduction

Plastic flow of metallic alloys subjected to various deformation conditions, including uniaxial tension/compression, torsion and multi-axial sheet forming, may display oscillatory plastic yielding under certain ranges of the applied loading rates and testing temperatures. When the instability occurs, if the test is run under constant applied stress rate ('soft' device) the typical stress–strain curve displays a wavy profile (*staircase type*), with bursts of plastic strain at almost constant stress, while if the test is driven under constant applied strain rate ('hard' device), the stress trace results serrated (*saw-tooth type*), with sudden stress drops at almost constant strain.

This irregular plastic flow is a form of material instability and associated loss of homogeneous deformation (strain localization), which is normally referred to as 'serrated flow' or 'repetitive yielding', sometimes as Savart–Masson or, more commonly in the physical metallurgy community, as Portevin–Le Chatelier (PLC) effect (Portevin and Le Chatelier, 1923). The literature on the PLC effect is vast. Comprehensive reviews on the subject comprising detailed referencing on the various aspects of the PLC effect, including experiments and modeling, are those provided e.g. by Bell (1973), p. 41-44 and 649-666, which presents a chronological outline of the earlier developments on the subject starting from those of Savart and Masson, by Neuhäuser (1990), by the Viewpoint Set 21 of *Scripta Metallurgica et Materialia*, Vol. 29 (1993), see Estrin et al. (1993), and, more recently, by Estrin and Kubin (1995) and Zaiser and Hähner (1997).

The PLC effect is basically understood as a material property since it is primary known to arise from the underlying microstructural processes governing the plastic deformation kinetics of metallic solid solutions, namely the dynamic interaction between gliding dislocations and mobile solute atoms. These local phenomena are referred to as Dynamic Strain Ageing (DSA) (see e.g. Cottrell, 1953; Baird, 1973; van den Beukel, 1975) and may induce a macroscopic negative Strain Rate Sensitivity (SRS) of the flow stress, that is a decrease of the flow stress at an increasing applied strain rate. This ultimately results macroscopically in plastic oscillations of the stress trace and in localized plastic straining.

As opposed to inhomogeneous plastic yield phenomena due to *strain-softening (Lüders bands)*, that may be handled by appropriate pre-deformation, the unstable plastic flow due to *strain-rate-softening (PLC bands)* does not occur only at once, but is rather repetitive. Then, the PLC range needs to be avoided in the industrial processes (e.g. sheet forming in automotive industry) to prevent the appearance of surface markings and waviness caused by the plastic oscillations.

Different types of PLC instabilities can be observed depending on the spatio-temporal organization of the deformation bands. Type C bands appear almost at random in the sample without propagating (stochastic nucleation), Type B bands exhibit an oscillatory or intermittent propagation along the tensile axis (stop-and-go), and Type A bands, finally, propagate continuously and smoothly (solitary plastic waves). This classification was mainly based on the types of serrations displayed by the stress–strain curves (Cuddy and Leslie, 1972; Pink and Grinberg, 1981; McCormick, 1986; Chihab et al., 1987; McCormick et al., 1993; Kalk and Schwink, 1995): Type A bands give rise to regular equi-distanced stress drops, Type C bands induce an heavily serrated flow with fine low amplitude oscillations, and Type B bands display additional oscillations as those of Type C superimposed on those characteristic of pure Type A. However, this phenomenological classification cannot be considered fully conclusive, since similar stress–strain serrations may arise from very different space–time patterns of strain localization. This has been concluded from detailed laser-extensometric observations at the scale where the inhomogeneous deformation takes place (Ziegenbein, 2000; Hähner et al., 2002), as well as from the numerical modeling of the present PLC model (Rizzi and Hähner, 2002).

The existing models of the PLC instability, e.g. Penning (1972), Kubin and Estrin (1985), McCormick (1988), Zbib and Aifantis (1988), Estrin and Kubin (1991), Mesarovic (1995), Hähner (1993), (1996), cannot be considered to be fully satisfactory because they lack in practice a proper physical identification of the critical material parameters associated to the PLC instability and, mainly, they fail to predict correctly the kinematics characteristics of the PLC bands, namely the band propagation speed, the band width and the plastic strain carried by the band. Previous studies specifically devoted to investigate the kinematics of PLC bands have been reported by Chihab et al. (1987), Zbib and Aifantis (1988), McCormick et al. (1993), Hähner (1993), Jeanclaude and Fressengeas (1993), Dablij and Zeghloul (1997). However, there are still open debated aspects, as for example that of the (increasing or decreasing) trend experienced by the band speed at increasing applied stress or strain rate (see e.g. McCormick et al., 1993; Estrin and Kubin, 1995, p. 47, and Zaiser and Hähner, 1997, p. 316). Here the band speed is found to grow (non-linearly) with the increase of the applied strain rate.

The characterization of the band parameters is the main concern of the present paper, which aims at a consistent determination of the band characteristics on both theoretical and numerical grounds. A model of the PLC effect is presented, which attempts to bridge the microstructural aspects of DSA with the macroscopic mechanical behaviour associated with the PLC instability. The model is coupled in time and (one-dimensional) space and introduces in the evolution equations two intrinsic time scales corresponding to the two competing processes of the DSA kinetics (dislocation pinning by the solute clouds and thermal activation of the arrested dislocations), and a characteristic length scale through a diffusion-like space coupling term with spatial second-order gradient (accounting for the long-range dislocations interactions).

The model has been formalized and described in details in Hähner et al. (2002) and in Rizzi and Hähner (2002). The main constitutive equations and analytical derivations of the PLC model are here summarized first (Section 2). Approximate analytical solutions are also recalled for the boundaries of the PLC range and for the strain localization characteristics defining the kinematics of the PLC deformation bands. Then, these characteristics are validated by a systematic numerical analysis of Type A PLC bands for tensile tests simulated at different constant and variable applied cross-head velocities (Section 3). A parallel numerical investigation on the different types of spatio-temporal organization of the PLC bands is provided in Rizzi and Hähner (2002). Such simulations display very rich qualitative patterns of strain localization and corresponding phenomenological stress–strain responses. Overall, these numerical results are in full qualitative agreement with the experimental observation of the PLC effect in metal alloys. A first quantitative matching of the present model with the experimental results is attempted in Hähner et al. (2002) for a Cu-Al alloy.

2 Theoretical modeling

2.1 The model equations

The present model of the PLC effect is based on the two following evolution equations for the *plastic* strain rate $\varepsilon_{,t}$ and for the rate $(\Delta G)_{,t}$ of the additional activation enthalpy ΔG linked to

DSA (see Hähner et al., 2002; Rizzi and Hähner, 2002):

$$\begin{cases} \varepsilon_{,t} \;=\; \nu\,\Omega\,\exp\left[-\dfrac{G_0+\Delta G}{kT}+\dfrac{\sigma_{\rm ext}-\sigma_{\rm int}}{S_0}\right]\,, & (1)\\[2ex] (\Delta G)_{,t} \;=\; D\,\Delta G_{,xx}+\eta\,(\Delta G_\infty-\Delta G)-\dfrac{\varepsilon_{,t}}{\Omega}\,\Delta G\,. & (2)\end{cases}$$

The first Arrhenius-type equation (1) interprets plastic flow as a thermally-activated process of dislocation motion. Ω and ν are physical parameters representing the elementary plastic strain corresponding to the activation of all mobile dislocations and the attempt frequency of thermal activation; $k{=}1.38{\cdot}10^{-23}$ J/K is the Boltzmann constant and T the (constant) absolute temperature; $G{=}G_0{+}\Delta G$ is the Gibbs free activation enthalpy, with G_0 the constant activation enthalpy in the absence of DSA; $\sigma_{\rm eff}(\varepsilon,\varepsilon_{,t},\Delta G){=}\sigma_{\rm ext}(\varepsilon,\varepsilon_{,t},\Delta G){-}\sigma_{\rm int}(\varepsilon)$ is the effective stress available to propel dislocation motion, namely the difference between the externally applied stress $\sigma_{\rm ext}$ (flow stress) and the internal stress $\sigma_{\rm int}$ (back stress) resulting from other defects and linked to plastic strain hardening (quasi-linear strain hardening is assumed, $\sigma_{{\rm int},t}{=}h\,\varepsilon_{,t}$, with h a constant piece-wise linear hardening parameter); S_0 is the *instantaneous* SRS of the flow stress, an intrinsically-positive parameter, which is generally distinct from the *asymptotic* SRS S_∞ (see e.g. Zaiser and Hähner, 1997),

$$S_0=\left.\frac{\partial\,\sigma_{\rm ext}}{\partial\ln\varepsilon_{,t}}\right|_{\varepsilon,\,\Delta G};\quad S_\infty=\left.\frac{\partial\,\sigma_{\rm ext}}{\partial\ln\varepsilon_{,t}}\right|_{\varepsilon}=S_0+\left.\frac{\partial\,\sigma_{\rm ext}}{\partial\Delta G}\right|_{\varepsilon}\frac{{\rm d}\Delta G}{{\rm d}\ln\varepsilon_{,t}}=S_0\,\left(1+\frac{1}{k\,T}\,\frac{{\rm d}\Delta G}{{\rm d}\ln\varepsilon_{,t}}\right),\quad (3)$$

which represents the SRS of the flow stress for DSA processes that have relaxed to a new steady state. Taking the derivative ${\rm d}\Delta G/{\rm d}\ln\varepsilon_{,t}$ for $\Delta G{=}\Delta G_{\rm s}{=}\Delta G_\infty/(1+\varepsilon_{,t}/(\eta\Omega))$, namely the steady state value of the additional activation enthalpy corresponding to $(\Delta G)_{,t}{=}0$ in eqn (2), the asymptotic SRS of the model is evaluated as

$$S_\infty=S_0\,\left(1-\frac{\Delta G_\infty}{k\,T}\frac{\varepsilon_{,t}/(\eta\Omega)}{\Big(1+\varepsilon_{,t}/(\eta\Omega)\Big)^2}\right), \qquad (4)$$

and may become negative in the PLC range, provided that $\Delta G_\infty/(k\,T){>}4$.

The three terms in the evolution equation (2) interpret respectively the following phenomena: long-range dislocation interaction (diffusion-like coupling based on a spatial second-order gradient, e.g. Aifantis, 1984), ageing linked to dislocations pinning by the solute atoms, dislocations unpinning by thermal activation and consequent release of the solute cloud. D is the diffusion coefficient, with dimensions of $[L]^2/[t]$; ΔG_∞ is the maximum value of the additional activation enthalpy that can be induced by DSA; η^{-1} is the intrinsic time scale of the ageing process, which competes with the time scale $\Omega/\epsilon_{,t}$ linked to thermal activation.

To account for a spatially-extended system, the constitutive equations (1)-(2) must be complemented by the *'machine equation'*

$$\frac{\sigma_{\mathrm{ext},t}}{E_{\mathrm{eff}}} = \frac{v}{l} - \frac{1}{l} \int_0^l \varepsilon_{,t}\, \mathrm{d}x \ , \tag{5}$$

which expresses the additive composition of elastic and plastic deformation rates to comply with the imposed cross-head velocity v. Here $E_{\mathrm{eff}}{=}E\,E_{\mathrm{m}}/(E+E_{\mathrm{m}})$ is the effective elastic stiffness of the system composed of the specimen (Young's modulus E) and the tensile machine (elastic modulus E_{m}), and l is the parallel length of the specimen.

2.2 Qualitative response of the system

To simplify the model equations and reduce the number of independent parameters the PLC model (1)-(2) is better expressed in terms of non-dimensional variables:

$$\begin{cases} \dot{f} \ = \ \dot{\sigma} f - \theta \exp[-g]\, f^2 \ , & (6) \\ \dot{g} \ = \ g'' + g_\infty - g - f \exp[-g]\, g \ . & (7) \end{cases}$$

Here f plays the role of a non-dimensional driving force linked to the effective stress σ_{eff}, while g is the non-dimensional additional activation enthalpy:

$$f \equiv f_0 \exp\left[\frac{\sigma_{\mathrm{eff}}}{S_0}\right] \ , \quad f_0 \equiv \frac{\nu}{\eta} \exp\left[-\frac{G_0}{kT}\right] \quad ; \qquad g \equiv \frac{\Delta G}{k\,T} \ . \tag{8}$$

Accordingly, also $g_0{\equiv}G_0/(k\,T)$, $g_{\mathrm{s}}{\equiv}\Delta G_{\mathrm{s}}/(k\,T)$ and $g_\infty{\equiv}\Delta G_\infty/(k\,T)$. The overscored dot denotes the time derivative with respect to the non-dimensional time $\tilde{t}{=}\eta t$, namely $\dot{(\ )}{=}(\ )_{,t}/\eta$. The dimensionless stress rate $\dot{\sigma}$ and hardening coefficient θ are scaled parameters which relate to the actual stress rate $\sigma_{\mathrm{ext},t}$ and the strain hardening coefficient h as $\dot{\sigma}{=}\sigma_{\mathrm{ext},t}/(\eta S_0)$, $\theta{=}\Omega h/S_0$. The primes in g'' denote instead differentiation with respect to the non-dimensional spatial coordinate $\tilde{x}{=}\sqrt{\eta/D}\,x$, where $\sqrt{D/\eta}$ is a characteristic length linked to diffusion.

The non-dimensional hardening coefficient θ is assumed to be small: $\theta{\ll}1$ (*'weak hardening'*). In such case, the variable f can be considered as the 'slow' variable of the model, whereas g represents its 'fast' variable. The qualitative response of the constitutive model and associated PLC oscillations is based on a *'limit cycle'* behavior: the system orbits in the (g, f) plane around the (inaccessible) *'working point'* (f_s, g_s)

$$f_s = \frac{\dot{\sigma}}{\theta} \exp g_s \ , \qquad g_s = \frac{g_\infty}{1 + \dot{\sigma}/\theta} \ , \tag{9}$$

that represents the steady state values of both variables f and g ($\dot{f}$=$\dot{g}$=0), and must be taken on the unstable ascending branch of the $\dot{g}$=0 characteristic (Fig. 1).

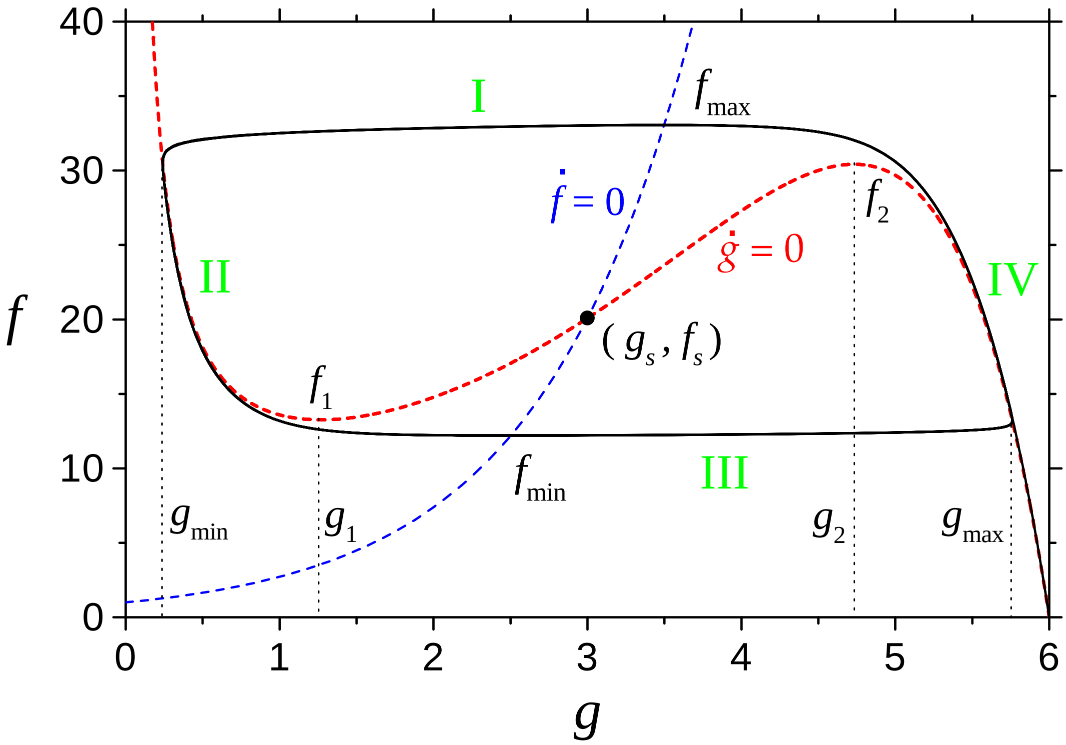

Figure 1: Representation of the limit cycle in the (g, f) plane for g_∞=6 and $\dot{\sigma}/\theta$= 1: g_s=3, f_s=e^3=20.08, g_1=1.27, g_2=4.73, f_1=13.26, f_2=30.42, g_{min}=0.24, g_{max}=5.76. The 'working point' (g_s,f_s) is taken on the unstable ascending branch of the $\dot{g}$=0 characteristic. The system orbit is divided into four phases (see also Fig. 2): I) dislocations unpinning from solute clouds, II) dislocations glide, III) dislocations recapture and pinning, IV) dislocations arrested.

The orbit on the limit cycle is divided into four phases. During phases I and III, the fast variable g oscillates rapidly but continuously at almost constant f and reaches respectively the minimum and maximum values of g, that is g_{min}, g_{max}. Otherwise the system stays very close to the $\dot{g}$=0 characteristic (phases II and IV), consistently with an adiabatic approximation of the ageing kinetics. To a first estimation, the amplitude of the limit cycle can be based on the *'switching curve approximation'*, that is by assuming that phases I and III take place with discontinuous jumps of g (at constant f) from the extrema of one stable branch to the other stable branch of the $\dot{g}$=0 characteristic. The values $f_{\min}$ and $f_{\max}$ can then be approximately estimated by f_1 and f_2, and $g_{\min}$, $g_{\max}$ are read accordingly on the $\dot{g}$=0 characteristic. For g_∞=6, namely the value assumed in subsequent computations, one gets g_1=1.27, g_2=4.73, f_1=13.26, f_2=30.42, while $g_{\min}$, $g_{\max}$ can be determined numerically as $g_{\min}$=0.24, $g_{\max}$=5.76.

The four phases of each orbit on the limit cycle have a corresponding physical meaning in the spatially-correlated response of the present material model. Each orbit on the limit cycle corresponds to the nucleation and subsequent propagation of a single PLC band travelling at constant speed $c_{\rm b}$ as a plastic wave along the specimen axis. Since for a solitary wave time and space derivatives are related by $f_{,t}$=$-c_{\rm b}\,f_{,x}$ and $g_{,t}$=$-c_{\rm b}\,g_{,x}$, the spatial profiles of the model variables f and g can be read-off from the time profiles by abscissa reversal. Fig. 2 sketches qualitatively the expected spatial profiles of the non-dimensional variables f and g, and of the plastic strain ε and plastic strain rate $\varepsilon_{,t}$ corresponding to a plastic strain burst travelling at speed $c_{\rm b}$. The four marked phases of the DSA kinetics correspond to those of the limit cycle and represent the following physical phenomena: I) unpinning of dislocations in front of the band; II) intermediate hardening with dislocation glide; III) recapturing of dislocations by the solute clouds in the wake of the band; IV) stress built-up during dislocation arrest preceding a new nucleation phase.

2.3 Negative SRS and PLC ranges

As already commented, the 'working point' of the unstable system must be taken on the (inaccessible) ascending branch of the $\dot{g}$=0 characteristic. Provided that g_∞>4, such curve is *'N-shaped'* (Penning, 1972) and the asymptotic SRS of the model, eqn (4), becomes negative for the *interval of the plastic strain rates leading to a negative asymptotic SRS*:

$$\frac{g_\infty - 2 - \sqrt{g_\infty(g_\infty-4)}}{2} < \frac{\varepsilon_{,t}}{\eta\Omega} < \frac{g_\infty - 2 + \sqrt{g_\infty(g_\infty-4)}}{2}\,. \tag{10}$$

For g_∞=6, the bounds (10) for a negative asymptotic SRS become (0.268, 3.732).

A first estimation of the PLC range can be made instead by a linear stability analysis signaling the onset of diverging perturbations around the steady state (*'Hopf bifurcation'*). Provided that g_∞>2+θ+2$\sqrt{1+\theta}\approx$4+2θ, the onset of this bifurcation leads to the *interval of plastic strain*

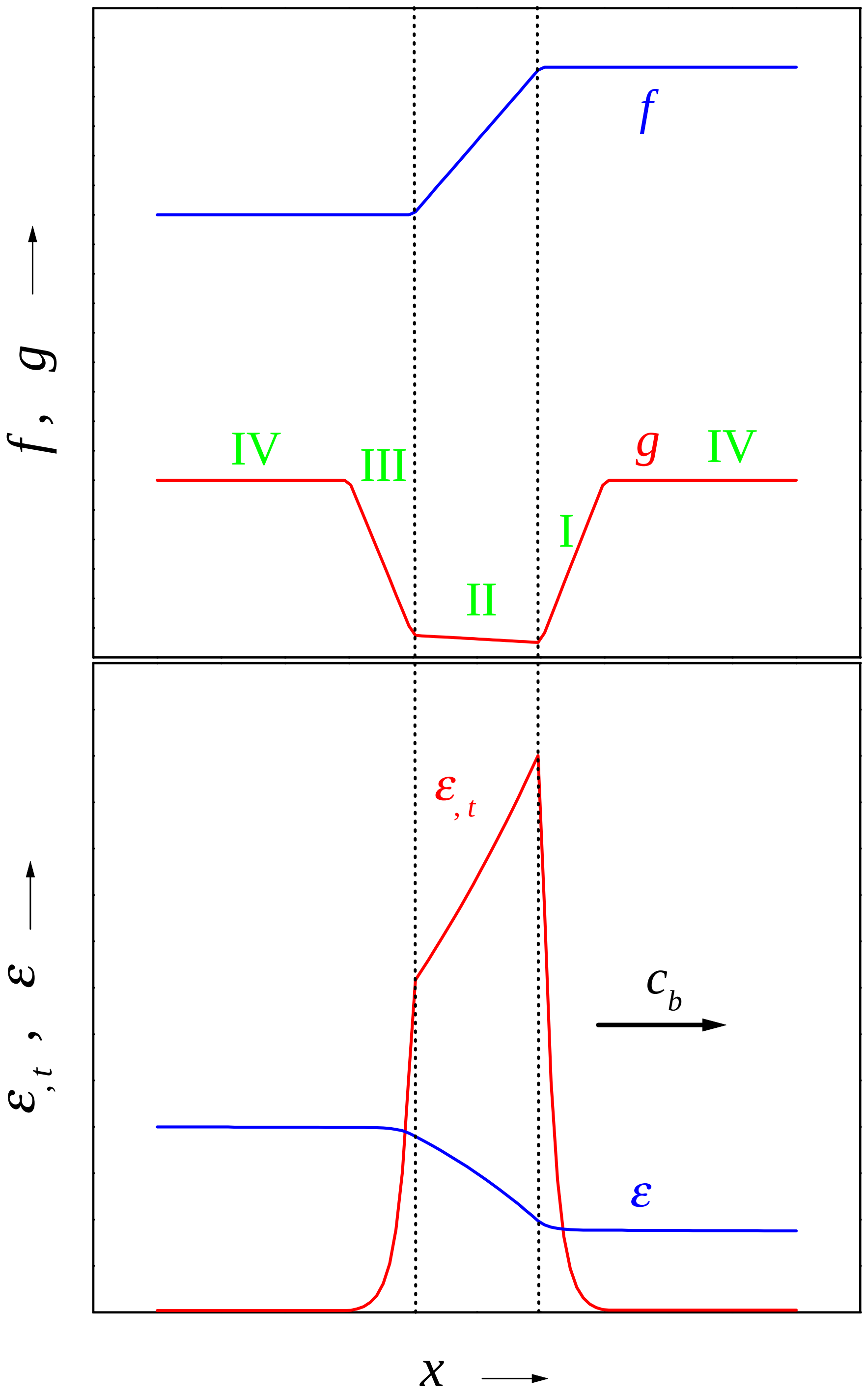

Figure 2: Plastic strain rate burst carried by a solitary plastic wave propagating in space (along x coordinate) with speed c_b: schematic representation of the spatial profiles of the non-dimensional variables f and g and of the corresponding plastic strain ε and plastic strain rate $\varepsilon_{,t}$. The four marked phases correspond to (see also Fig. 1): I) dislocations unpinning from solute clouds, II) dislocations glide, III) dislocations recapture and pinning, IV) dislocations arrested. Variations of f and ε mainly take place during phase II, while sharp variations of g and $\varepsilon_{,t}$ occur during phases I and III at almost constant f and ε. The corresponding temporal profiles result from abscissa reversal.

rates constituting the unstable PLC range:

$$\frac{g_\infty - 2 - \theta - \sqrt{(g_\infty - \theta)^2 - 4g_\infty}}{2(1+\theta)} < \frac{\epsilon_{,t}}{\eta\,\Omega} < \frac{g_\infty - 2 - \theta + \sqrt{(g_\infty - \theta)^2 - 4g_\infty}}{2(1+\theta)} \,. \tag{11}$$

The PLC range (11) is somehow narrower than that of the negative asymptotic SRS (10) due to the presence of the θ terms in eqn (11): plastic instability develops only for some finite negative value of S_∞. For example, for g_∞=6 and θ=0.01 the PLC bounds (11) become (0.269, 3.682). However, for weak hardening the two ranges almost coincide, since $\theta \ll 1$. On the other hand, the PLC range is expected to be broader than that estimated by linear perturbation, since the 'Hopf bifurcation' is 'subcritical', in the sense that the presence of noise has a destabilizing effect on the onset of the PLC instability. Indeed, while for g_∞=6 and $\theta \to 0$ eqn (11) provides the *plastic* strain rate range (0.268, 3.732)$\cdot$ 10^{-6} s^{-1} for the PLC effect, systematic numerical simulations scanning a series of applied cross-head velocities (Rizzi and Hähner, 2002) showed the PLC instability for *total* applied strain rates belonging to the interval (0.20, 5.70)$\cdot$ 10^{-6} s^{-1} (consider here that the difference attributable to the elastic strain rate is practically negligible).

2.4 Band kinematics characteristics

To estimate the kinematics characteristics of solitary plastic waves (Type A PLC bands), the two following simplifying assumptions can be made: (a) the band plastic strain $\Delta\varepsilon_{\rm b}$ can be considered to accommodate virtually the whole applied strain rate v/l. Then, relations $v{=}\Delta\varepsilon_{\rm b}\, c_{\rm b}$ and $v{=}\varepsilon_{{\rm b},t}\, w_{\rm b}$ link the applied cross-head velocity v to the propagation speed $c_{\rm b}$, the local plastic strain rate in the band $\varepsilon_{{\rm b},t}$ and the band width $w_{\rm b}$. This means that out of the three band characteristics $c_{\rm b},\, w_{\rm b},\, \Delta\varepsilon_{\rm b}$, only two are independent; (b) the dimensionless stress rate term $\dot\sigma$ in eqn (6) is appreciable only during the quasi-elastic deformation preceding the nucleation of a new band, while it can be neglected during the propagation of a fully developed band. Recalling that solitary wave solutions obey $\dot f{=}-c\, f'$ and $\dot g{=}-c\, g'$, where $c{=}c_{\rm b}/\sqrt{\eta D}$ now denotes the non-dimensional band speed, the set of band parameters can be derived for the limiting case $\theta \ll 1$. The derivation is reported in Hähner et al. (2002) and in Rizzi and Hähner (2002) and is repeated below for the sake of completeness.

Consider a uniformly propagating PLC band as described by the dimensionless rate equations (6), (7). Within the hypotheses above, eqns (6), (7) give

$$cf' - \theta \exp[-g]\, f^2 \;=\; 0 \;, \tag{12}$$

$$g'' + cg' - f \exp[-g]\, g + g_\infty - g \;=\; 0 \;. \tag{13}$$

To calculate c, eqn (13) is multiplied by g' and integrated along the tensile axis. Since the spatial profile is strongly localized, the integral over the specimen length l can be extended to $\pm\infty$. As g' vanishes at $\pm\infty$, this yields:

$$c = \frac{\displaystyle\int_{-\infty}^{+\infty} f g g' \exp[-g]\, \mathrm{d}x}{\displaystyle\int_{-\infty}^{+\infty} (g')^2\, \mathrm{d}x} = \frac{I_1}{I_2} \;. \tag{14}$$

Consider first the numerator I_1. Upon integrating by parts and inserting f' from eqn (12), one gets

$$I_1 = \frac{\theta}{c} \int_{-\infty}^{+\infty} (1+g)(f \exp[-g])^2\, \mathrm{d}x \;. \tag{15}$$

To evaluate this integral one notes that $f\exp[-g]{=}\varepsilon_{,t}/(\eta\Omega)$ is localized within the band width, with plastic strain rate in the band ruled by $g_{\min}$ (Fig. 2). Then I_1 is approximated by:

$$I_1 \approx \frac{\theta}{c}\, (1+g_{\min}) \left(\frac{\varepsilon_{\mathrm{b},t}}{\eta\Omega}\right)^2 w \;, \tag{16}$$

where $w{=}\sqrt{\eta/D}\, w_{\mathrm{b}}$ is the dimensionless band width. To evaluate the denominator I_2, according to the ‘switching-curve approximation’, one may decompose the deformation band profile into three substages, $w{=}w_{\mathrm{I}}{+}w_{\mathrm{II}}{+}w_{\mathrm{III}}$ (Fig. 2). As g' is negligible in Stage II (where $g{\approx}g_{\min}$), the denominator of eqn (14) can be approximated by

$$I_2 \approx (g_{\max} - g_{\min})^2 \left(\frac{1}{w_{\mathrm{I}}} + \frac{1}{w_{\mathrm{III}}}\right) \approx 2(g_{\max} - g_{\min})^2 \;, \tag{17}$$

where unity widths (that is the characteristic length defined by the diffusion-like coupling) have been assumed for substages I and III, $w_{\mathrm{I}}{\approx}w_{\mathrm{III}}{\approx}1$, for self-consistency. To estimate w_{II}, one may use the adiabatic approximation $g'{\approx}g''{\approx}0$ in eqn (13), $f\exp[-g]{\approx}g_\infty/g-1{\approx}g_\infty/g_{\min}{-}1$, and integrate eqn (12) to arrive at $c\,\ln[f_{\max}/f_{\min}]{=}\theta(g_\infty/g_{\min}{-}1)w_{\mathrm{II}}$. According to the definition of f, eqn (8), by neglecting again the stress rate term, one gets

$$\Delta\varepsilon_{\mathrm{b}} = \frac{\Omega}{\theta}\; \ln\left[\frac{f_{\max}}{f_{\min}}\right] \;, \tag{18}$$

and therefore

$$w_{\mathrm{II}} = \frac{g_{\min}}{g_\infty - g_{\min}}\,\frac{v}{\Omega\sqrt{\eta D}}\ . \tag{19}$$

Note that eqn (18) relates the band plastic strain $\Delta\varepsilon_{\mathrm{b}}$ to the amplitude of the limit cycle ruled by $f_{\max}$, $f_{\min}$. Also, note that in eqn (19), the actual value of the hardening coefficient θ has dropped out. Finally, upon combining eqns (16)-(19) and returning to dimensional units, the following set of band parameters is obtained:

$$\begin{cases} c_{\mathrm{b}} = \left(\dfrac{D}{\eta}\right)^{1/4} \dfrac{\sqrt{(1+g_{\min})/2}}{g_{\max}-g_{\min}}\,\sqrt{\theta}\,\dfrac{v}{\Omega\sqrt{w_{\mathrm{b}}}}\ , & (20) \\ w_{\mathrm{b}} = 2\sqrt{\dfrac{D}{\eta}} + \dfrac{g_{\min}}{g_\infty - g_{\min}}\,\dfrac{v}{\eta\Omega}\ , & (21) \\ \Delta\varepsilon_{\mathrm{b}} = \dfrac{v}{c_{\mathrm{b}}} = \dfrac{g_{\max}-g_{\min}}{\sqrt{(1+g_{\min})/2}}\,\dfrac{\Omega}{\left(\dfrac{D}{\eta}\right)^{1/4}}\,\dfrac{\sqrt{w_{\mathrm{b}}}}{\sqrt{\theta}}\ . & (22) \end{cases}$$

Notice that the band speed c_{b} depends non-linearly on the applied cross-head velocity v, through eqns (20) and (21). Moreover, eqn (20) predicts a square root dependence of c_{b} on the non-dimensional hardening coefficient θ. The faster the material hardens, the higher is the band speed, while conversely the lower is the plastic strain carried by the band, eqn (22). The characteristic length $\sqrt{D/\eta}$ (up to a factor 2) represents the intrinsic length introduced into the model by the diffusion term and prevents the band width w_{b}, eqn (21), to tend to zero as $v{\to}0$. The second term of w_{b}, linear in v, is bounded from above only by the upper boundary value corresponding to that of the cross-head velocity in the PLC range (see also comments in the Conclusions in connection with geometrical factors linked to the specimen size). The dependence of the three band parameters with θ and v, specifically the trend that $c_{\mathrm{b}}\ \sqrt{w_{\mathrm{b}}/\theta}$ scales linearly with v, and the assumptions made in the theory, e.g. that $c_{\mathrm{b}}\Delta\varepsilon_{\mathrm{b}}{\approx}v$, is now going to be validated numerically in the next section by systematic numerical simulations of Type A band propagation in the PLC range.

3 Numerical modeling

A throughout investigation of the band characteristics of Type A PLC bands is now performed. The adopted model parameters are the following: η=0.1 s^{-1}, Ω=10^{-5}, S_0=1 MPa, E=E_m=10^5 MPa ($E_{\rm eff}$=$0.5\ 10^5$ MPa), $f_{(0)}$=f_0=10^{-13} (initial yield limit at around 100/3 MPa), $g_{(0)}$=g_∞=6 (infinitely-aged material before testing), D=10^{-7} m^2/s or D=$4 \cdot 10^{-7}$ m^2/s, l=0.1 m. The strain hardening coefficient is either taken constant, θ=θ_0=$\Omega h_0/S_0$ (linear strain hardening), with h_0 assuming values between 200 and 1000 MPa, or linearly dependent with the space-average plastic strain ε_{av} (parabolic strain hardening), θ=$\theta_0$$-2 \cdot 10^{-6}$ ε_{av}, where here θ_0=0.01 is the initial non-dimensional hardening coefficient corresponding to h_0=1000 MPa.

The governing equations are discretized both in time and in space and solved through a Finite Differences integration scheme on the space coordinate at each discrete time instant. A non-dimensional time step $\Delta\tilde{t}$=0.1 and a density of 100 spatial segments (‘blocks’) along the specimen length have been considered. Fixed boundary conditions have been assumed, namely, $\dot{f}$=$\dot{g}$=0 at the specimen extremities for each discrete time instant. To trigger the PLC instability, the initial condition $f_{(0)}$ is perturbed at the second block by a random multiplicative factor varying between 1 and 30, which alters locally the yield strength up to a maximum of about 10%.

To allow a simultaneous representation of both global (stress-time curves) and local responses (space–time fields of the plastic strain rate), the band propagation is traced graphically in the space–time plane by using two-dimensional localization maps that mark the successive space–time locations undergoing a local maximum of the plastic strain rate. The band data are filtered out automatically from the space–time plastic fields of $\varepsilon_{,t}$ and ε: the band speed is evaluated from the slopes of the band traces in the space–time localization maps, the band width is estimated from the extension (either in space or in time) of the base of the plastic strain rate spikes, and the band plastic strain is evaluated from the steps of the corresponding plastic strain–time profiles.

3.1 Uniaxial tension tests at constant applied strain rates in the PLC range

We present first the results of a series of simulated tensile tests at constant applied cross-head velocities in the PLC range with imposed parabolic strain hardening. Typically, the Type A PLC bands display a very smooth propagation mode with reflection at the specimen boundaries and result in a corresponding wavy staircase profile of the flow stress trace. Such band propagation with reflection pattern is sometimes denoted as Type A2 (Kalk and Schwink, 1995) or Type D (McCormick et al., 1993), while more classical Type A bands, sometimes referred to as Type A1 (Kalk and Schwink, 1995), always nucleate at the same end of the specimen and propagate in the same direction, with a corresponding serrated profile of the flow stress.

3.1.1 Uniaxial tension test at constant cross-head velocity v=0.50 $\cdot$ 10^{-7} m/s in the PLC range

The global and local responses of the system are first shown in Figs. 3-4: Fig. 3a reports the space–time localization map, together with the relevant imposed hardening–time and resulting post-yield stress–time curve; Fig. 3b depicts the stress–strain curve and again the imposed hardening coefficient of parabolic plastic strain hardening. Fig. 3 shows Type A2 band propagation and the associated staircase stress trace with horizontal steps increasing in time and strain, and vertical stress steps of decreasing magnitude as hardening decreases. Fig. 4 represents the time evolution of the plastic strain rate and plastic strain as recorded at one half the specimen length. Fig. 4a shows the response during the entire loading history, occurring with repeated bursts of plastic activity at the time instants in which the PLC band reaches the central gauge and with corresponding staircase steps of the plastic strain. Notice the smooth time profiles, that can be better appreciated in Fig. 4b, where a zoom window near the end of the loading history is represented.

The characteristics of the PLC deformation bands are reported in Fig. 5 as a function of the hardening coefficient θ: Fig. 5a depicts the band maximum plastic strain rate and the band plastic strain (compare also to Fig. 4); Fig. 5b represents the band speed and the band width. Notice that the band width is practically constant, in accordance with the prediction from the theory, eqn (21), for a test driven under constant applied strain rate. Notice also the quite regular variations of band speed and band plastic strain as captured by the present model and by the numerical procedures developed to filter out automatically the band kinematics data. These first trends of the dependencies of the band parameters are already in good agreement with the approximate theoretical estimations (20)-(22). The square root dependence of the band speed with hardening is better identified next.

3.1.2 Comparison of uniaxial tension tests with different cross-head velocities *v*=0.30 $\cdot$ $10^{-7}\div$ 1.20 $\cdot$ 10^{-7} m/s in the PLC range

To validate the square root dependence of the band speed with the hardening coefficient, further numerical tests have been run with different cross-head velocities in the PLC range, namely v=(0.30, 0.50, 0.60, 0.80, 1.00, 1.20) $\cdot$ 10^{-7} m/s. Fig. 6 reports the recorded band speeds as a function of the imposed hardening coefficient θ; Fig. 6a shows a standard double-linear plot, while Fig. 6b represents the dependence in a double-log plot. The range of variation of the band speed is more reduced for the slowest applied strain rate (v=0.30 $\cdot$ 10^{-7} m/s) since Type A PLC bands appear only towards the end of the loading history, while Type C bursts prevail in the first nucleation phase (see also numerical results presented in Rizzi and Hähner, 2002). As a difference to all other cases, for the highest applied strain rate (v=1.20 $\cdot$ 10^{-7} m/s) a propagation pattern with renucleation always at the same end of the specimen and propagation towards the other end was recorded (Type A1) instead of the reflection pattern (Type A2). This does not basically affect the estimation of the band parameters, while rather changes the stress–time profile, which is observed to be serrated at regular intervals (trace really typical of Type A PLC bands), rather than of staircase type.

Fittings of the c_{b} dependence with θ are better evaluated linearly in the double-log plot of Fig. 6b. The results are in very good agreement with the square root dependence predicted by the theory, eqn (20), since the range of the θ dependence exponent is found to be between 0.49 and 0.56. Higher scatter from the 0.5 slope is observed towards the higher applied strain rates, especially for the highest value, which gave rise to the non-reflective localization pattern as mentioned above. On the basis of these numerical tests it can be concluded that the band speed predicted by the present PLC model scales approximately well with the square root of the hardening coefficient, as estimated by theory.

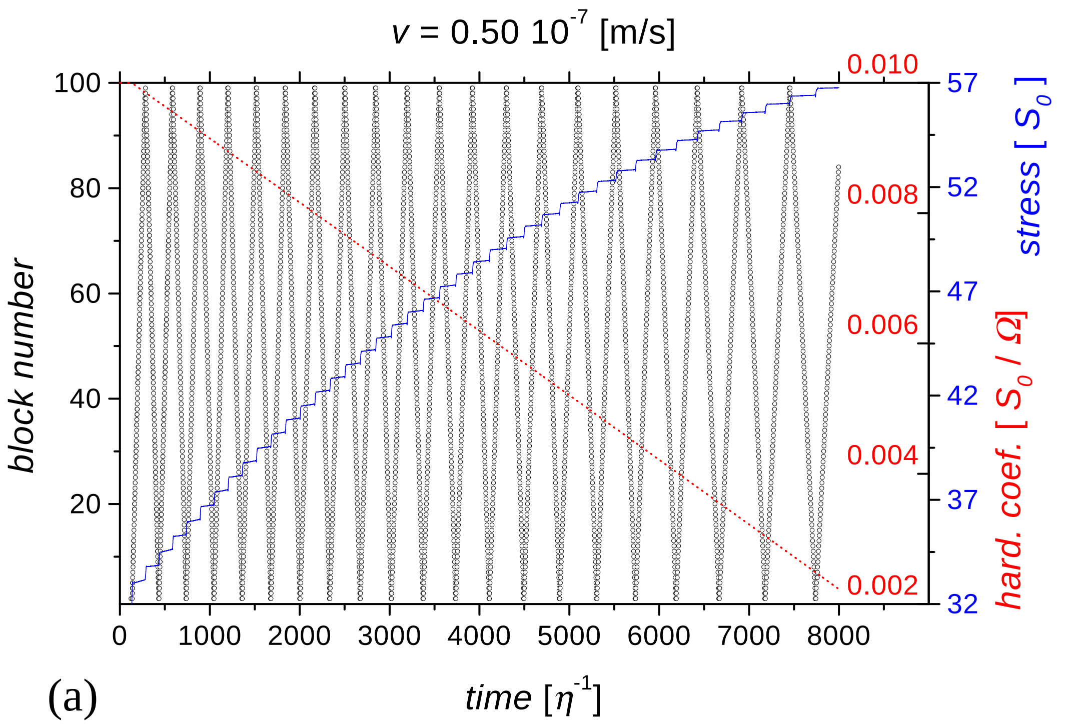

(a)

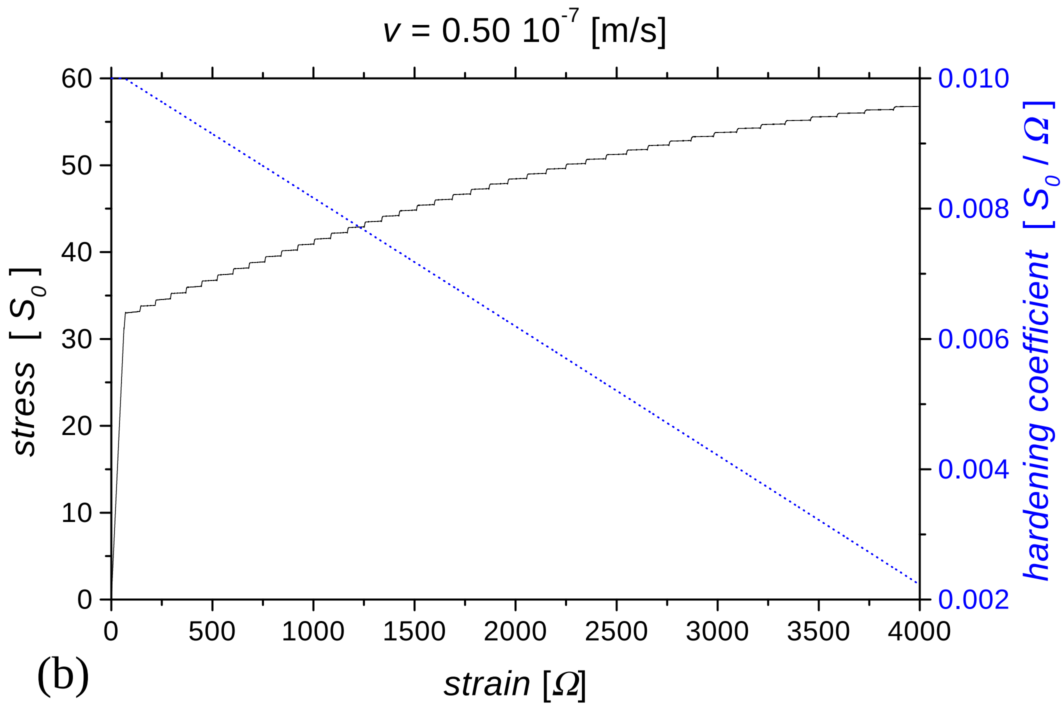

(b)

Figure 3: Uniaxial tension test simulated at constant applied cross-head velocity in the PLC range $(0.20\div5.70)\cdot10^{-7}$ *m/s,* v*=0.50* $\cdot10^{-7}$ *m/s (*η*=0.1 s*$^{-1}$*,* S_0*=1 MPa,* Ω*=*10^{-5}*): (a) space–time localization map (left axis, scatter plot with circles), hardening–time (right axis, left ticks, dotted line) and stress–time curve (right axis, right ticks, continuous line); (b) stress–strain curve (left axis, continuous line) and imposed hardening coefficient of parabolic plastic strain hardening vs. strain (right axis, dotted line).*

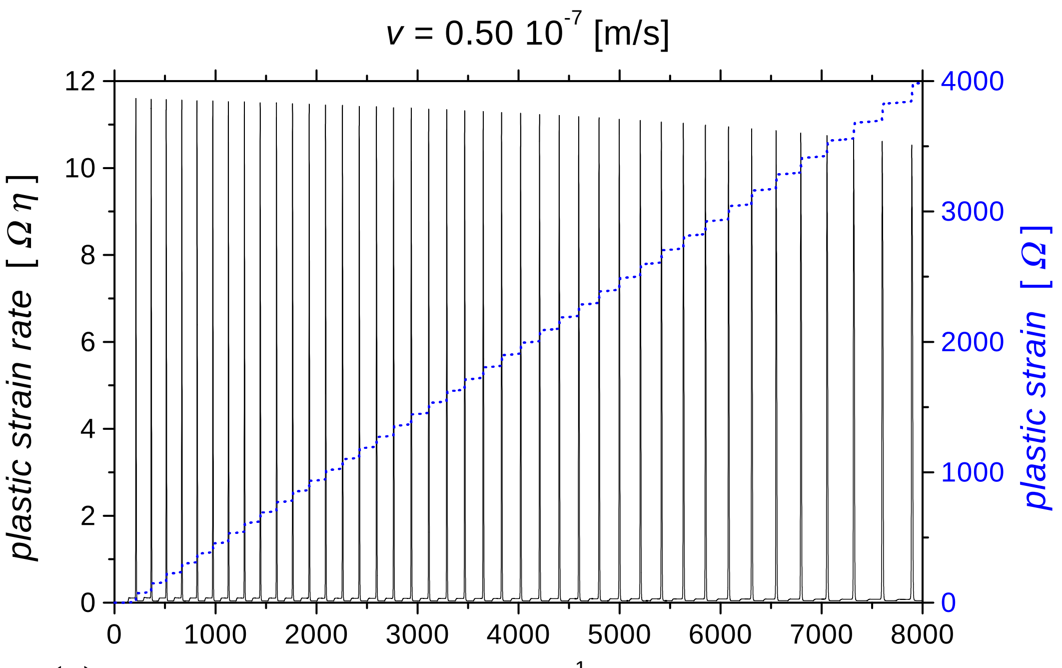

(a)

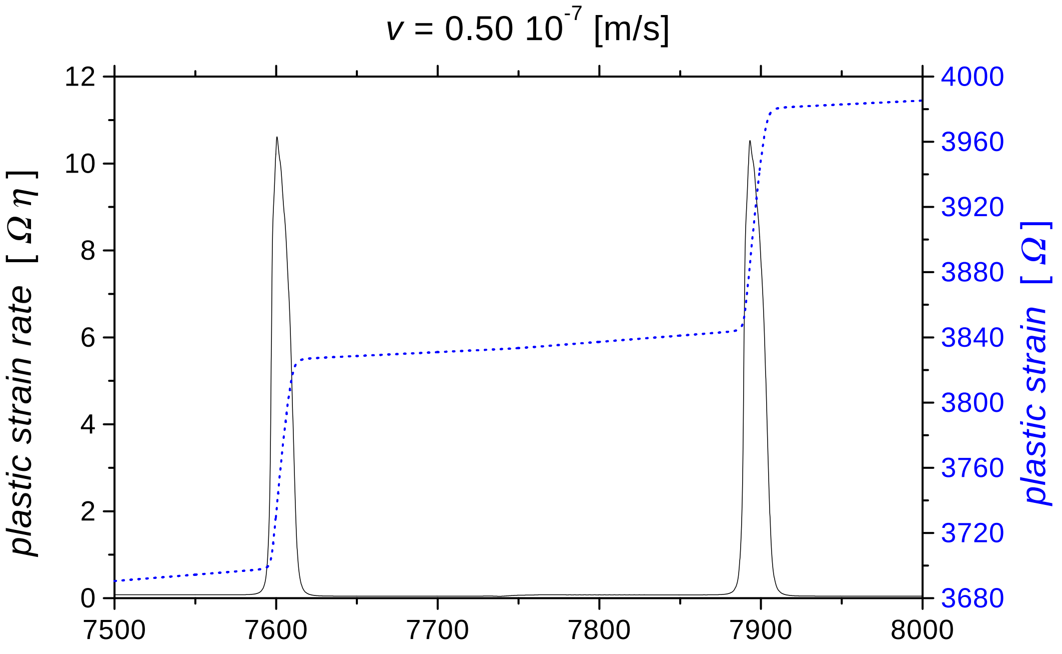

(b)

Figure 4: Uniaxial tension test simulated at constant applied cross-head velocity in the PLC range (0.20÷5.70) $\cdot\ 10^{-7}$ m/s, v=0.50 $\cdot\ 10^{-7}$ m/s (η=0.1 s^{-1}, Ω=10^{-5}). Plastic strain rate (left axis, continuous line) and plastic strain (right axis, dotted line) vs. time at one half the specimen length; (a) full response and (b) zoom at the end of the loading history showing two plastic strain rate bursts and the corresponding plastic strain steps.

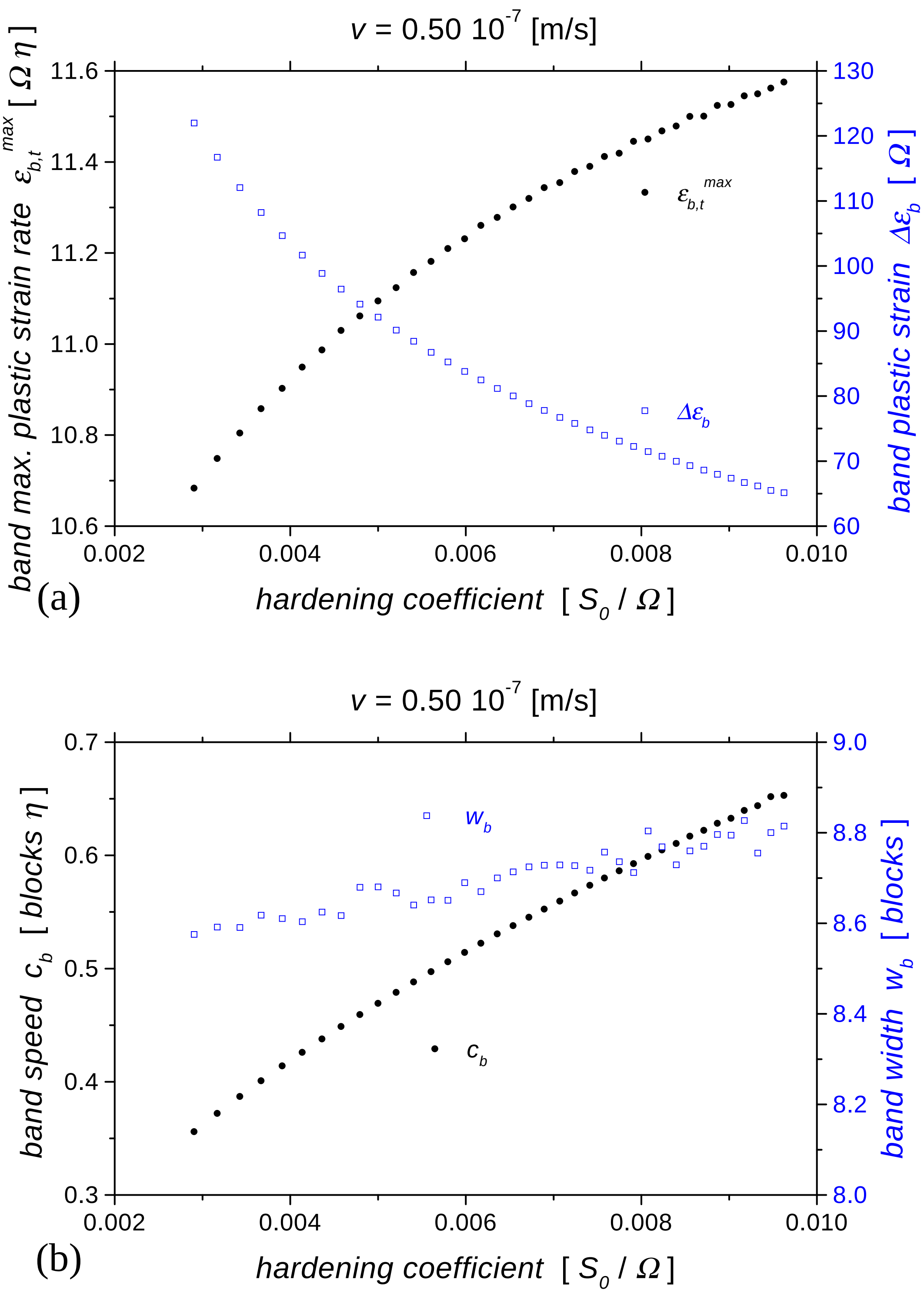

Figure 5: Uniaxial tension test simulated at constant applied cross-head velocity in the PLC range (0.20÷5.70) $\cdot\ 10^{-7}$ m/s, v=0.50 $\cdot\ 10^{-7}$ m/s (η=0.1 s^{-1}, S_0=1 MPa, Ω=10^{-5}). Band characteristics as a function of hardening coefficient θ: (a) band max. plastic strain rate $\varepsilon_{\mathrm{b},t}^{\max}$ (left axis, solid marks) and band plastic strain $\Delta\varepsilon_{\mathrm{b}}$ (right axis, open marks); (b) band speed c_{b} (left axis, solid marks) and band width w_{b} (right axis, open marks).

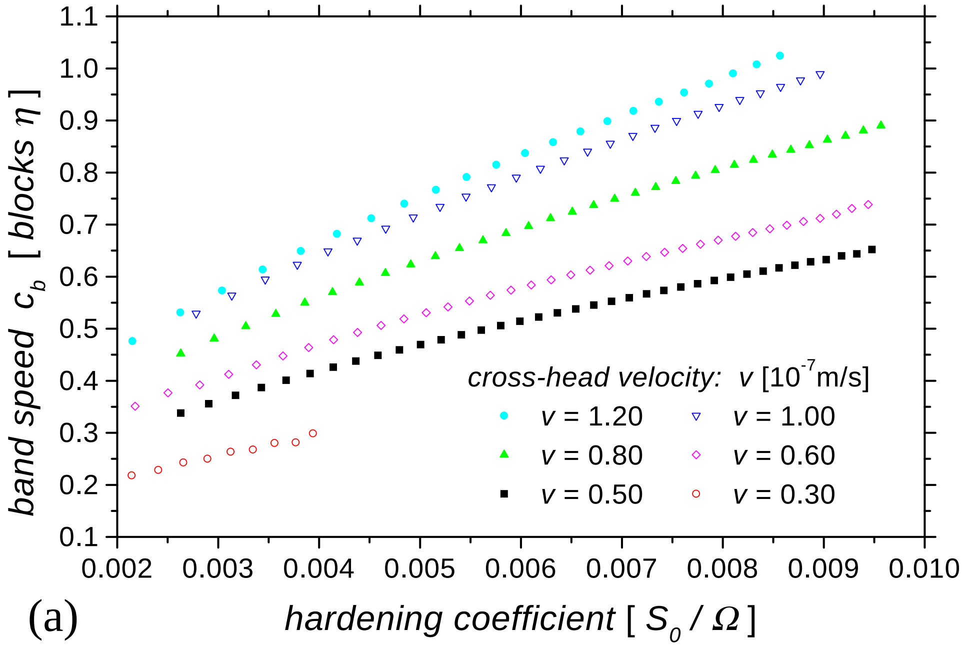

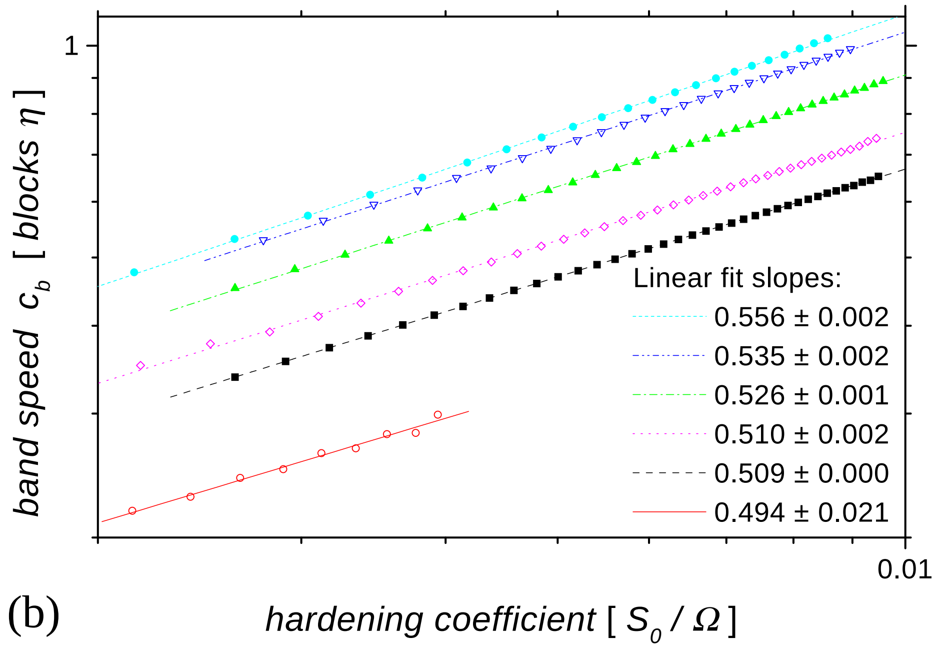

Figure 6: Uniaxial tension test simulated at constant applied cross-head velocity in the PLC range (0.20÷5.70) · 10^{-7} m/s, v=(0.30, 0.50, 0.60, 0.80, 1.00, 1.20) · 10^{-7} m/s (η=0.1 s^{-1}, S_0=1 MPa, Ω=10^{-5}). Band speed c_b as a function of hardening coefficient θ: (a) double-linear plot; (b) double-log plot with linear fittings.

3.2 Uniaxial tension tests with linear ramp of the applied strain rate in the PLC range

To investigate further the dependence of the band parameters with the applied cross-head velocity v, a series of simulated tensile tests run at linearly-increasing applied cross-head velocity is performed. The hardening coefficients are taken here constant (linear hardening). The imposed cross-head velocity varies between v_0=0.30 $\cdot$ 10^{-7} m/s and v=3.00 $\cdot$ 10^{-7} m/s, according to the following linear ramp of the applied strain rate $\dot{\epsilon}{=}v/l$: $\dot{\epsilon}{=}\dot{\epsilon}_0{+}2.7{\cdot}10^{-10}\,\tilde{t}$, where $\tilde{t}$ is the non-dimensional time. The applied strain rate ramp can be seen in Fig. 7, which is presented next.

3.2.1 Uniaxial tension tests at constant hardening coefficient *h*=200 MPa

Fig. 7a presents the space–time localization map, together with the relevant post-yield stress–time curve and the linear ramp of the applied strain rate; Fig. 7b shows the flow stress and the applied strain rate vs. strain. The typical pattern of the stress–strain curve consistent with reflective propagation shifts from staircase to wavy type, with horizontal steps of magnitude decreasing in time and increasing in strain.

Propagation is once again very smooth, which allows for a convenient filtering of the band parameters. The band characteristics are displayed in Fig. 8 as a function of the applied strain rate $\dot{\epsilon}{=}v/l$. Fig. 8a represents the band width together with a linear fit that has to be compared with the approximate analytical prediction (21). Fig. 8b depicts both the band speed and the band plastic strain. The scatter plot of the band speed is also fitted with the non-linear expression predicted by theory, eqn (20), where the two parameters fixing the linear dependence of the band width are taken from the previous fit in Fig. 8a. This fitting renders a power exponent around -0.52 in very good agreement with the inverse square root dependence with -0.5 power. The fitted parameters apply also to the plot of the band plastic strain through eqn (22).

The influence of the diffusion coefficient D on the band characteristics is studied next (Fig. 9). Two different runs with D=1$\cdot$ 10^{-7} m^2/s and 4 $\cdot$ 10^{-7} m^2/s are compared. Fig. 9a depicts the band width vs. the applied strain rate $\dot{\epsilon}{=}v/l$. According to eqn (21) the influence of D could be read through the offsets difference of the linear fittings. Since D is four times higher, the offset for the higher value of D should be twice the offset for the lower value of D.

The ratio between the two offsets of about 7.11/3.63=1.96 is quite in good agreement with such prediction. The slight difference in the slopes of the two fittings may be explained in terms of the increase of g_{min} for higher D. Fig. 9b represents the band speed times the square root of the band width vs. the applied strain rate $\dot{\epsilon}$=v/l. In this case the influence of D should be read through the different slopes of the linear fittings, which should differ by a factor of $\sqrt{2}$. The ratio obtained from the plots, 2.47/1.62=1.52, is actually a bit higher. Such difference should be also explained in terms of the increase of g_{min} induced by the stronger spatial coupling.

3.2.2 Comparison of uniaxial tension tests with different constant hardening coefficients *h*=100 $\div$ 1000 MPa

A last series of numerical tests is performed for a full validation of the analytical prediction of the band characteristics. Different runs with the linear ramp in the applied strain rate at different constant strain hardening coefficients h=100, 200, 300, 500, 1000 MPa have been carried out, with results summarized in Figs. 10-13.

Fig. 10 reports the band width as a function of the applied strain rate $\dot{\epsilon}$=v/l. All the data collapse rather well on the linear fitting, in agreement with eqn (21). Slight deviations are recorded only for the lowest and highest strain hardening coefficients. Fig. 11 shows the different non-linear variations of the band speed with the applied strain rate at changing hardening coefficient. This plot clearly shows qualitatively the increase of the band speed with both the applied strain rate and the hardening coefficient. The regular variations are quite remarkable, except for some deviations for the lowest hardening coefficient. Fig. 12 shows the variation of the plastic strain carried by the band, with similar increase trend with increasing applied strain rate, but with converse decreasing trend at increasing hardening coefficient.

In sum, as the material is plastically softer, the PLC band becomes slower but carries a larger plastic strain. The variations are very regular, except once again for the case with smallest hardening coefficient. This run experienced indeed some deviations from the regular pattern with smooth Type A2 propagation with boundary reflection, similarly to what that starts to be seen near the specimen boundaries for h=200 MPa in the localization map of Fig. 7. The qualitative trends of band speed increase with the applied cross-head velocity are in agreement with the findings in McCormick et al. (1993).

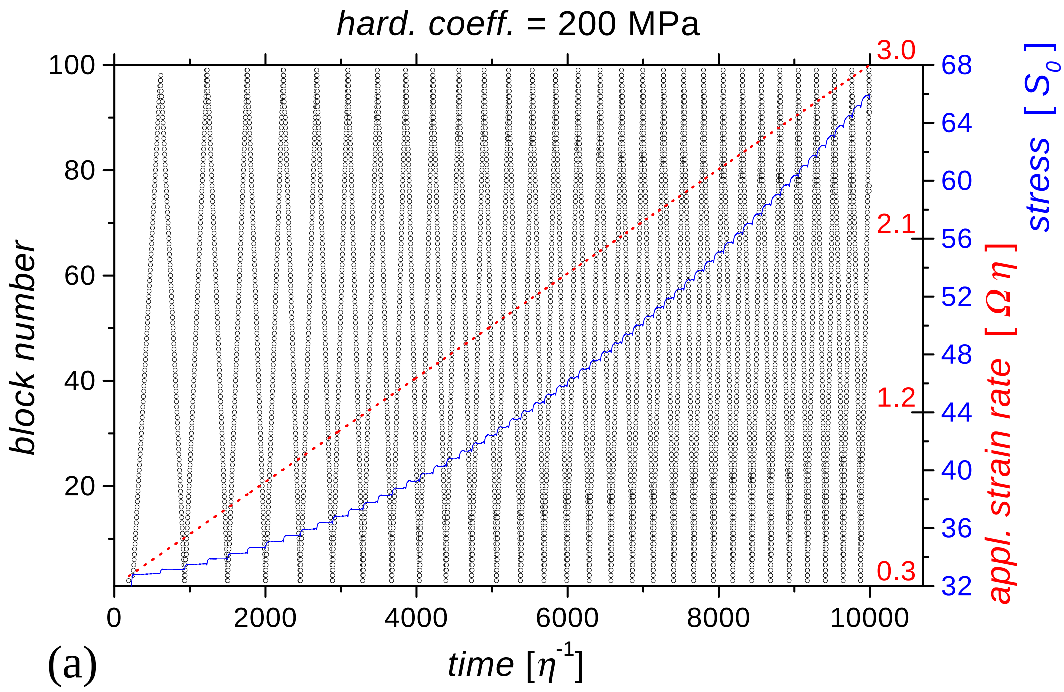

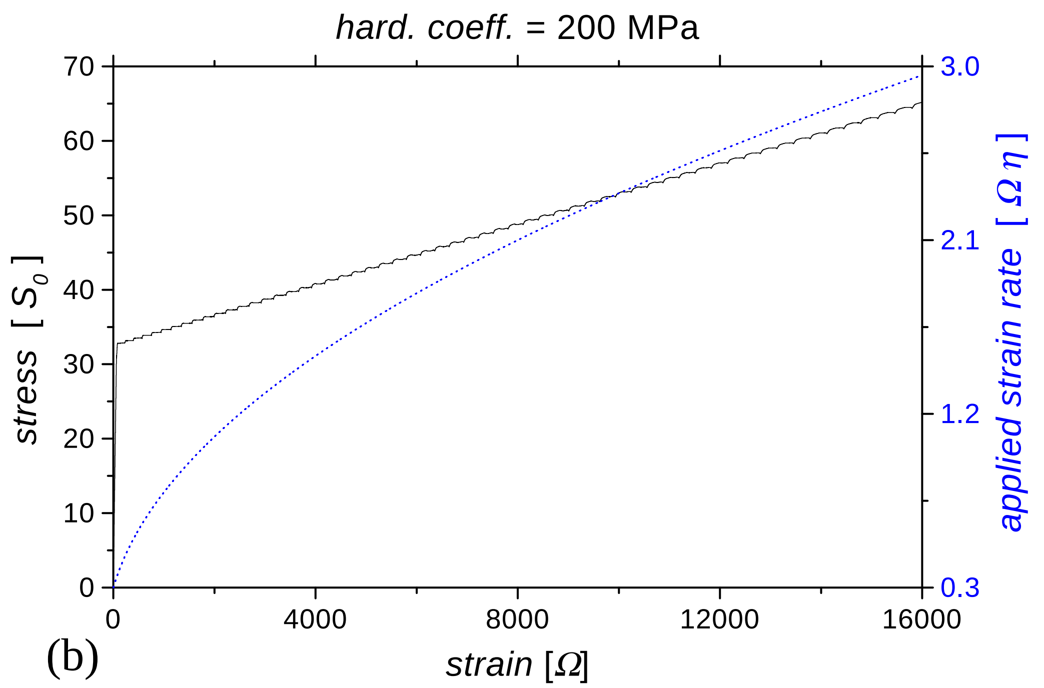

Figure 7: Uniaxial tension test simulated at linearly increasing applied cross-head velocity, v=(0.30÷3.00) · 10^{-7} m/s, and constant strain hardening, h=200 MPa (η=0.1 s^{-1}, S_0=1 MPa, $\Omega=10^{-5}$): (a) space–time localization map (left axis, scatter plot with circles), applied strain rate–time (right axis, left ticks, dotted line) and stress–time curve (right axis, right ticks, continuous line); (b) stress–strain curve (left axis, continuous line) and applied strain rate vs. strain (right axis, dotted line).

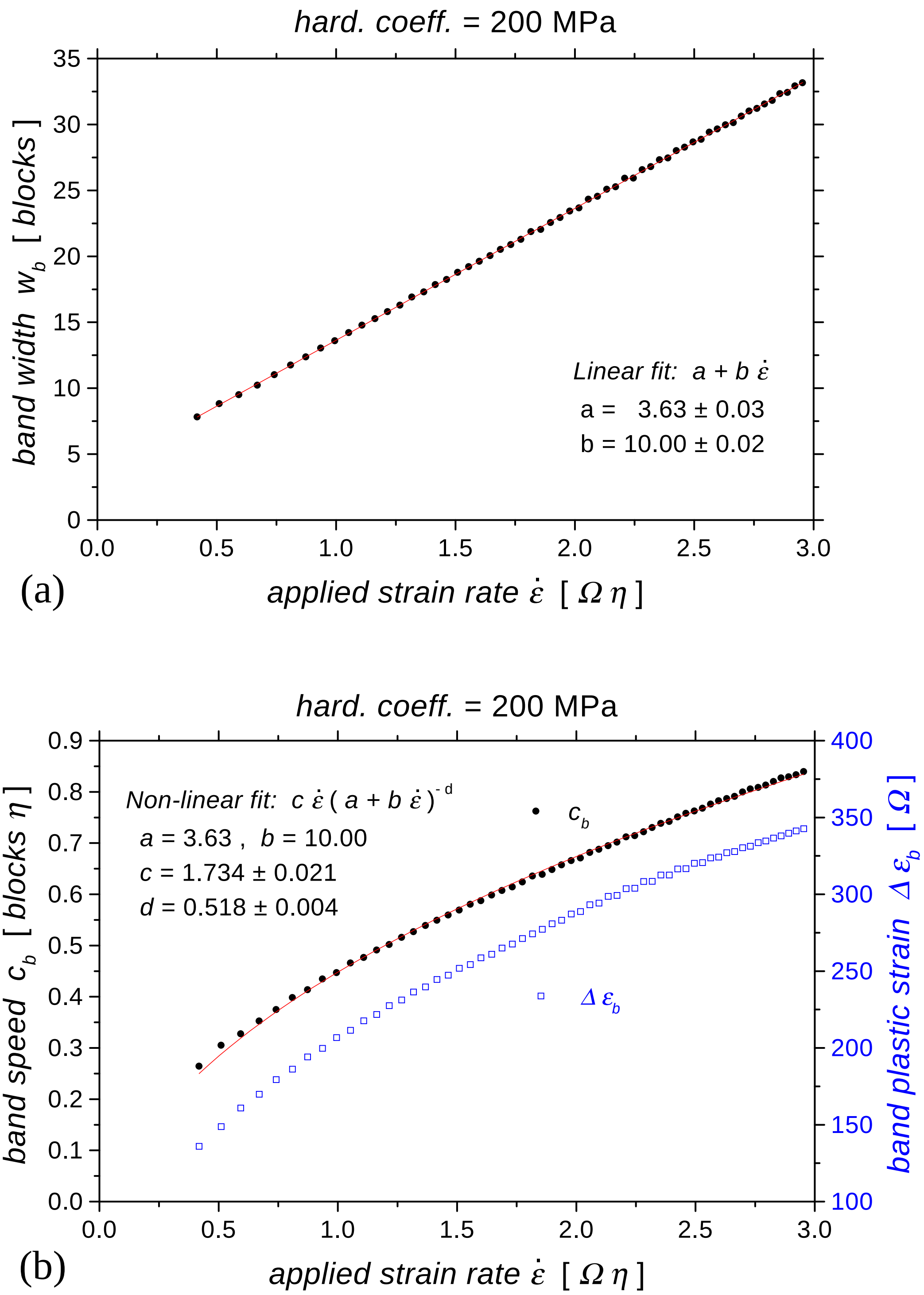

Figure 8: Uniaxial tension test simulated at linearly increasing applied cross-head velocity, v=(0.30÷3.00) · 10^{-7} m/s, and constant strain hardening, h=200 MPa (η=0.1 s^{-1}, Ω=10^{-5}). Band characteristics as a function of applied strain rate $\dot{\epsilon}=v/l$: (a) band width $w_{\rm b}$ with linear fit; (b) band speed $c_{\rm b}$ (left axis, solid marks and fitted curve) and band plastic strain $\Delta\varepsilon_{\rm b}$ (right axis, open marks).

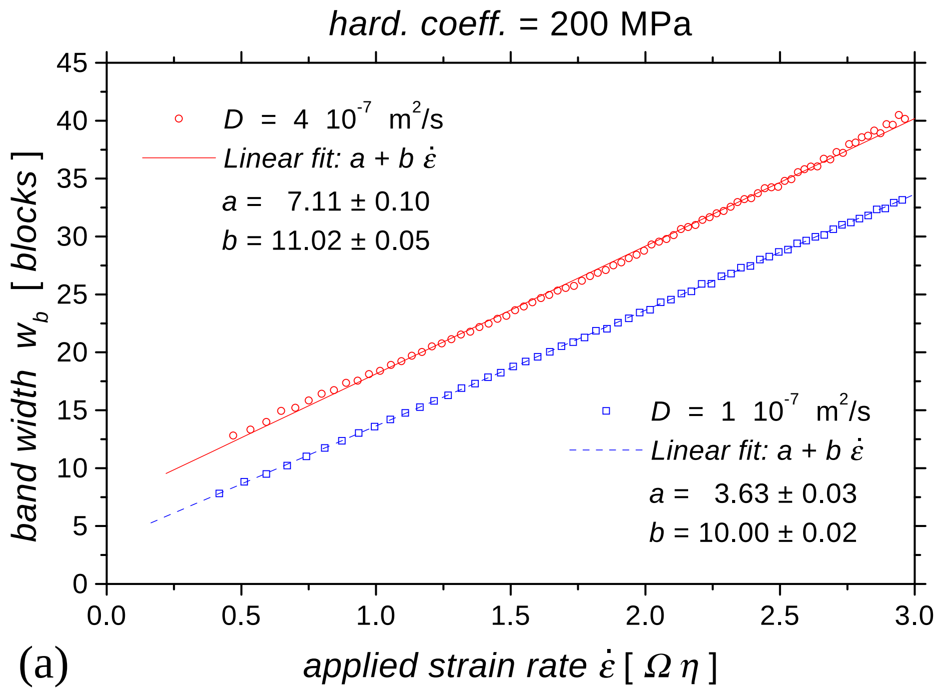

(a)

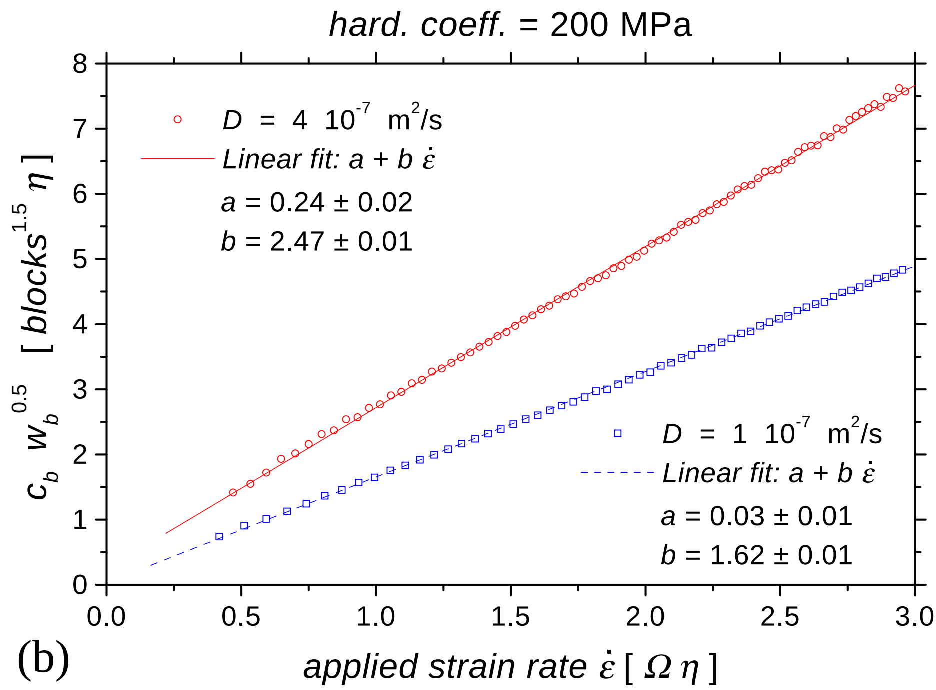

(b)

Figure 9: Uniaxial tension test simulated at linearly increasing applied cross-head velocity, v=(0.30÷3.00) · 10^{-7} m/s, and constant strain hardening, h=200 MPa (η=0.1 s^{-1}, Ω=10^{-5}). Influence of the diffusion coefficient D (see eqns (20), (21)): band characteristics vs. applied strain rate $\dot{\epsilon}=v/l$ for the two values D=(1, 4) · 10^{-7} m^2/s: (a) band width w_b; (b) band speed c_b times square root of band width w_b. The influence of D should be read on the linear fittings in (a) by the offsets difference, in (b) by the slopes difference.

Finally, Fig. 13 summarizes the numerical results for a better direct comparison with the analytical predictions from the theory. In Fig. 13a the quantity $c_{\rm b}\,\sqrt{w_{\rm b}/\theta}$ is plotted, which, according to eqn (20), should scale on the same linear relation with v for all hardening coefficients. The numerical results are in very good agreement with the theoretical prediction. This adds merit to the theoretical derivation since the scaling laws as derived here were not certainly easy to be foreseen a priori. A slightly more dispersed accumulation of markers is recorded for the quantity $c_{\rm b}\,\Delta\varepsilon_{\rm b}$ (Fig. 13b), that should basically render the applied cross-head velocity v. Actually, the only set which shows a slight deviation is that of the lowest hardening coefficient, since, as already commented, the corresponding profile of $\Delta\varepsilon_{\rm b}$ is not as regular as the other ones. However, a good linear dependence of the whole set of points is recorded with very satisfactory matching of the fitted slope. Notice that the small offsets apparent from the linear fittings are due to the elastic contributions, neglected in the theory. For example, the negative offset that can be read in Fig. 13b is consistent with the contribution of strain rate due to elastic effects that subtract from the total strain rate to give the strain rate relevant to the plastic activity.

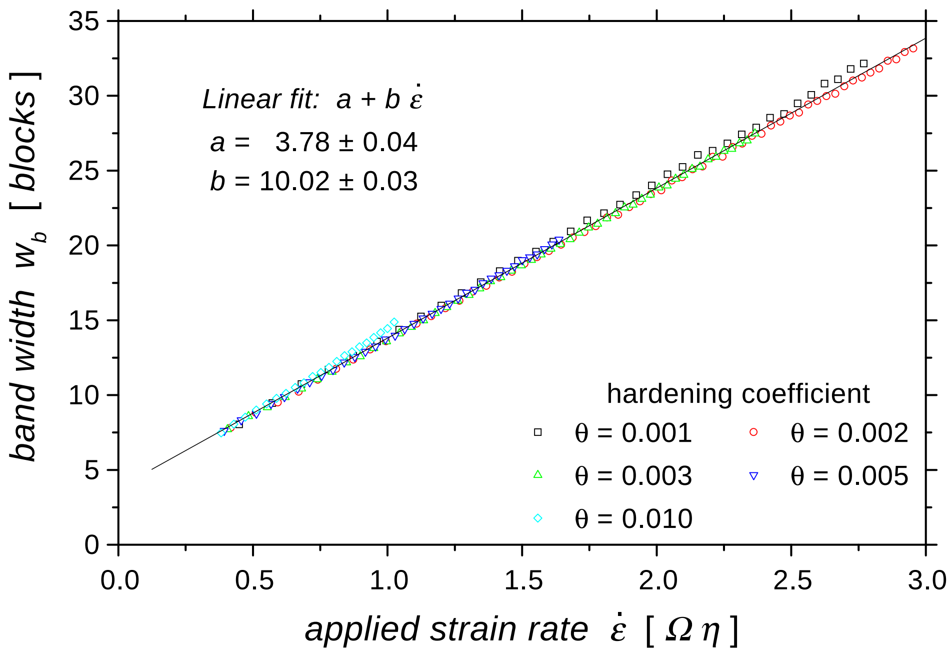

Figure 10: Uniaxial tension test simulated at linearly increasing applied cross-head velocity, v=(0.30÷3.00) · 10^{-7} m/s, at different constant strain hardening coefficients: h=100, 200, 300, 500, 1000 MPa (η=0.1 s^{-1}, Ω=10^{-5}). Band width $w_{\rm b}$ as a function of applied strain rate $\dot\epsilon$=v/l and linear fit.

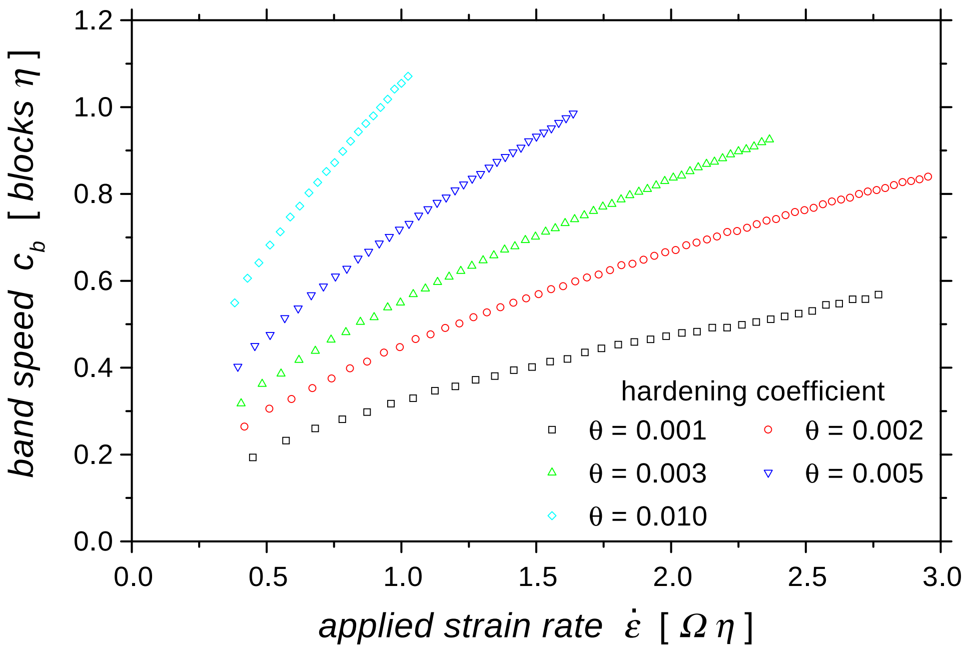

Figure 11: Uniaxial tension test simulated at linearly increasing applied cross-head velocity, v=(0.30÷3.00) · 10^{-7} m/s, at different constant strain hardening coefficients: h=100, 200, 300, 500, 1000 MPa (η=0.1 s^{-1}, Ω=10^{-5}). Band speed $c_{\rm b}$ as a function of applied strain rate $\dot{\epsilon}=v/l$.

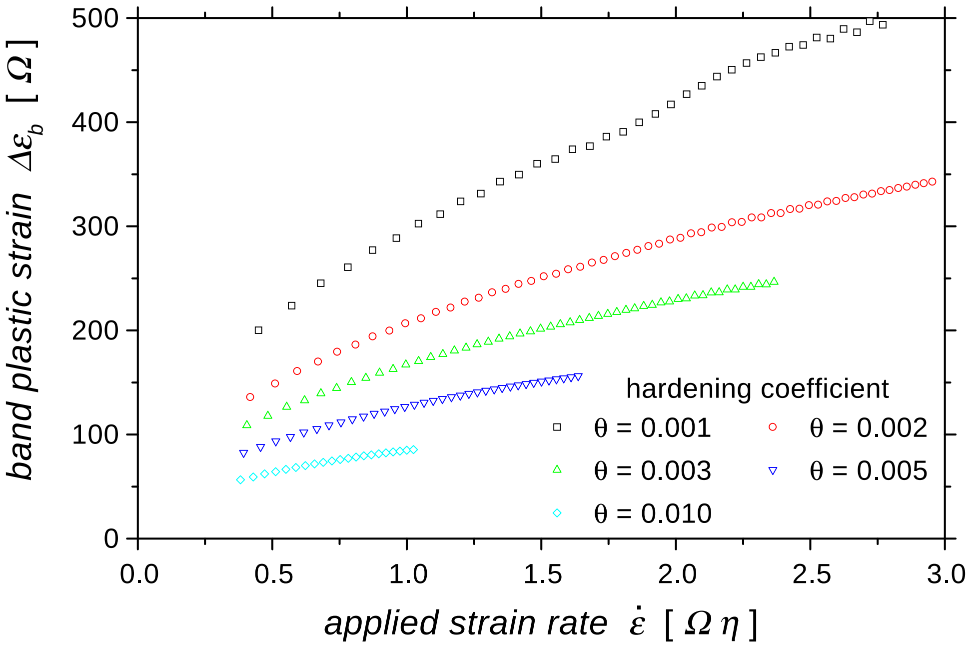

Figure 12: Uniaxial tension test simulated at linearly increasing applied cross-head velocity, v=(0.30÷3.00) · 10^{-7} m/s, at different constant strain hardening coefficients: h=100, 200, 300, 500, 1000 MPa (η=0.1 s^{-1}, Ω=10^{-5}). Band plastic strain $\Delta\varepsilon_{\rm b}$ as a function of applied strain rate $\dot{\epsilon}=v/l$.

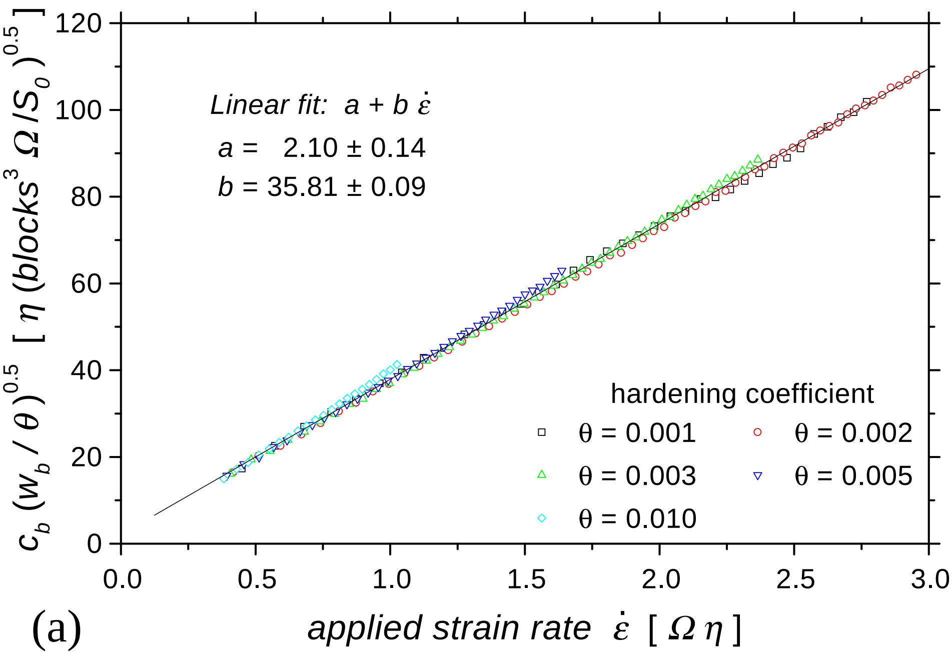

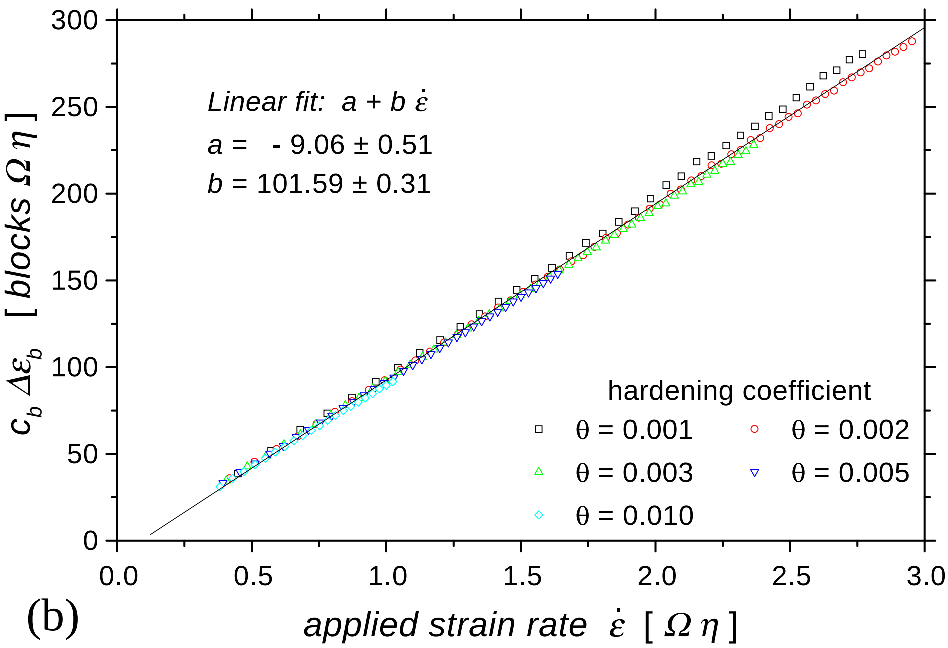

Figure 13: Uniaxial tension test simulated at linearly increasing applied cross-head velocity, v=(0.30÷3.00) $\cdot$ 10^{-7} m/s, at different constant strain hardening coefficients: h=100, 200, 300, 500, 1000 MPa (η=0.1 s^{-1}, S_0=1 MPa, Ω=10^{-5}). Checks of linear dependencies with the applied strain rate $\dot{\epsilon}$=v/l as predicted by the theory, eqns (20)-(22): (a) $c_\mathrm{b}\ \sqrt{w_\mathrm{b}/\theta} \approx v$; (b) $c_\mathrm{b}\ \Delta\varepsilon_\mathrm{b} \approx v$. The small offsets apparent from the linear fittings are due to the elastic contributions, neglected in the theory.

4 Conclusions

The present model of the PLC effect attempts a realistic macroscopic description of the spatio-temporal dynamics of PLC deformation bands associated with the kinetics of DSA. The predictive power of the present model has been explored analytically and numerically in a one-dimensional context, with specific reference to the propagation of solitary plastic waves, i.e. PLC bands of Type A. The numerical results are consistent with the analytical derivations and self-support the hypotheses made in the approximate evaluation of the band characteristics.

Further numerical results on the different PLC band patterns, including those of Type B and C and of multiple band propagation with 'accordion modes' (Type A'), are given in Rizzi and Hähner (2002). Additional numerical investigations with random perturbations of the local driving force at selected time steps and with sudden jumps in the applied strain rate are reported in Rizzi and Hähner (2001). Analytical derivations for the kinematics of Type B and C PLC bands are developed in Hähner et al. (2002). In the same paper, the order-of-magnitude agreement of physical parameters with experimental observation as experienced here and in Rizzi and Hähner (2002) is further supported by a first quantitative matching of the model prediction capabilities with the experimental findings for a Cu-Al alloy. Further quantitative matchings could be made possible once richer databases on the kinematics parameters will be available.

The influence of specimen geometry and size (e.g. specimen thickness) and the boundary conditions on the determination of the band parameters is not considered here. These aspects have a crucial impact on the overall kinematical behavior of the system. For example, the linear grow of the band width at increasing applied cross-head velocity as modeled here is bounded from above only by the value of band width corresponding to the upper applied strain rate in the PLC range. So, there is no correlation between such high values of the estimated band width and the specimen thickness, whereas the latter is known to bound the width of the PLC band. This calls for a more general multi-dimensional formulation of the model equations and relevant numerical analyses of the PLC effect, e.g. based on the Finite Elements Method. Such possible prosecution of the present research should allow to check further the model response and finally access the real prediction capabilities of this PLC model in simulating industrial applications connected with significant mechanical and technological implications of the PLC effect.

Acknowledgments

The authors are grateful for the financial support received from the European Commission under the TMR project on ‘Spatio-Temporal Instabilities in Deformation and Fracture’ (E.R.) and from a Heisenberg grant by the Deutsche Forschungsgemeinschaft (P.H.).

References

[1] Aifantis, E.C. (1984). On the microstructural origin of certain inelastic models. *J. of Engineering Materials and Technology*, ASME, **106**(4), 326-330.

[2] Baird, J.D. (1973). Dynamic Strain Aging. In *The Inhomogeneity of Plastic Deformation*, American Society of Metals, Metals Park, Ohio, USA.

[3] Bell, J.F. (1973). The Experimental Foundations of Solid Mechanics. *Encyclopedia of Physics*, Eds. S. Flügge and C. Truesdell, Mechanics of Solids I, Vol. VIa/1, Springer-Verlag, Berlin.

[4] Chihab, K., Estrin, Y., Kubin, L.P. and Vergnol, J. (1987). The kinetics of the Portevin–Le Chatelier bands in an Al-5at%Mg alloy. *Scripta Metallurgica*, **21**, 203-208.

[5] Cottrell, A.H. (1953). *Dislocations and Plastic Flow in Crystals*. University Press, Oxford.

[6] Cuddy, L.J. and Leslie, W.C. (1972). Some aspects of serrated yielding in substitutional solid solutions of iron. *Acta Metallurgica*, **20**, 1157-1167.

[7] Dablij, M. and Zeghloul, A. (1997). Portevin–Le Chatelier plastic instabilities: characteristics of deformation bands. *Materials Science and Engineering A*, **237**, 1-5, 1997.

[8] Estrin, Y. and Kubin, L.P. (1991). Plastic instabilities: phenomenology and theory. *Materials Science and Engineering A*, **137**, 125-134.

[9] Estrin, Y., Kubin, L.P. and Aifantis, E.C. (1993). Introductory remarks to the viewpoint set on propagative plastic instabilities. *Scripta Metallurgica et Materialia*, Viewpoint Set 21, **29**, 1147-1150.

[10] Estrin, Y. and Kubin, L.P. (1995). Spatial Coupling and Propagative Plastic Instabilities. In *Continuum Models for Materials with Microstructures*, Ed. H.B. Mühlhaus, 395-453, Wiley, New York.

[11] Hähner, P. (1993). Modelling the spatio-temporal aspects of the Portevin–Le Châtelier effect. *Materials Science and Engineering A*, **164**, 23-34.

[12] Hähner, P. (1996). On the physics of the Portevin–Le Châtelier effect, Part 1: The statistics of dynamic strain ageing, Part 2: From microscopic to macroscopic behaviour. *Materials Science and Engineering A*, **207**, 208-215, 216-223.

[13] Hähner, P., Ziegenbein, A., Rizzi, E. and Neuhäuser, H. (2002). Spatio-temporal analysis of Portevin-Le Châtelier deformation bands: theory, simulation and experiment. *Physical Review B*, **65**(13), Art. nr. 134109, 20 pages.

[14] McCormick, P.G. (1986). Dynamic strain ageing. *Transactions of the Indian Institute of Metals*, **39**, 98-106.

[15] McCormick, P.G. (1988). Theory of flow localisation due to dynamic strain ageing. *Acta Metallurgica*, **36**(12), 3061-3067.

[16] McCormick, P.G., Venkadesan, S. and Ling, C.P. (1993). Propagative instabilities: an experimental view. *Scripta Metallurgica et Materialia*, Viewpoint Set 21, **29**, 1159-1164.

[17] Mesarovic, S. DJ. (1995). Dynamic strain aging and plastic instabilities. *J. of the Mechanics and Physics of Solids*, **43**(5), 671-700.

[18] Neuhäuser, H. (1990). Plastic instabilities and the deformation of metals. In *Patterns, Defects and Material Instabilities*, Eds. D. Walgraef and N.M̃. Ghoniem, Kluwer Academic Publishers, 241-276.

[19] Kalk, A. and Schwink, Ch. (1995). On dynamic strain ageing and the boundaries of stable plastic deformation studied on Cu-Mn polycrystals. *Philosphical Magazine A*, **72**(2), 315-339.

[20] Kubin, L.P. and Estrin, Y. (1985). Portevin–Le Chatelier effect in deformation with constant stress rate. *Acta Metallurgica*, **33**(3), 397-407.

[21] Jeanclaude, V. and Fressengeas, C. (1993). Propagating pattern selection in the Portevin–Le Châtelier effect. *Scripta Metallurgica et Materialia*, Viewpoint Set 21, **29**, 1177-1182.

[22] Penning, P. (1972). Mathematics of the Portevin–Le Chatelier effect. *Acta Metallurgica*, **20**, 1169-1175.

[23] Pink, E. and Grinberg, A. (1981). Serrated flow in a ferritic stainless steel. *Materials Science and Engineering*, **51**(1), 1-8.

[24] Portevin, A. and Le Chatelier, F. (1923). Sur un phénomène observé lors de l'essai de traction d'alliages en cours de transformation. *Comptes Rendus de l'Academie des Sciences*, Paris, **176**, 507-510.

[25] Rizzi, E. and Hähner, P. (2001). "Theoretical analysis and numerical modelling of Portevin-Le Châtelier deformation bands". *XV AIMETA Congress of Theoretical and Applied Mechanics*, Taormina, Italy, Sept. 26-29, 2001, CD-ROM Proc., 10 pages.

[26] Rizzi, E. and Hähner, P. (2002). On the Portevin–Le Chatelier effect: theoretical modeling and numerical results. *Int. J. of Plasticity*, accepted.

[27] van den Beukel, A. (1975). Theory of the effect of dynamic strain ageing on mechanical properties. *physica status solidi (a)*, **30**, 197-206.

[28] Zaiser, M. and Hähner, P. (1997). Oscillatory modes of plastic deformation: theoretical concepts. *physica status solidi (b)*, **199**, 267-330.

[29] Zbib, H.M. and Aifantis, E.C. (1988). On the localization and postlocalization behaviour of plastic deformation. III. On the structure and velocity of the Portevin–Le Chatelier bands. *Res Mechanica*, **23**, 293-305.

[30] Ziegenbein, A. (2000). *Laserextensometrische Untersuchungen des Portevin–Le Châtelier-Effekts an einer CuAl-Legierung*. Doctoral Dissertation, Technische Universität Braunschweig, IMNF, D-38106 Braunschweig, Deutschland, Cuvillier Verlag, Göttingen.

Dipartimento di Ingegneria – Technical Reports

Numeri Recenti – Recent Issues